LAWRENCE
LIVERMORE
NATIONAL
LABORATORY

LLNL-JRNL-684087

Lineshape spectroscopy with a very high resolution, very high signal-to-noise crystal spectrometer

P. Beiersdorfer, E. W. Magee, G. V. Brown, H. Chen, J. Emig, N. Hell, M. Bitter, K. W. Hill, P. Allan, C. R. D. Brown, M. P. Hill, D. J. Hoarty, L. M. R. Hobbs, S. F. James

February 24, 2016

Review of Scientific Instruments

Disclaimer

Lineshape spectroscopy with a very high resolution, very high signal-to-noise crystal spectrometer

P. Beiersdorfer,[1] E. W. Magee,[1] G. V. Brown,[1] H. Chen,[1] J. Emig,[1] N. Hell,[1,2] M. Bitter,[3] K. W. Hill,[3] P. Allan,[4] C. R. D. Brown,[4] M. P. Hill,[4] D. J. Hoarty,[4] L. M. R. Hobbs,[4] and S. F. James[4]

[1)] *Lawrence Livermore National Laboratory, Livermore, CA 94550, USA*

[2)] *Dr. Remeis-Sternwarte & ECAP, Universität Erlangen-Nürnberg, 96049 Bamberg, Germany*

[3)] *Princeton Plasma Physics Laboratory, Princeton, New Jersey 08543, USA*

[4)] *Directorate of Research and Applied Science, AWE plc, Reading RG7 4PR, UK*

We have developed a high-resolution x-ray spectrometer for measuring the shapes of spectral lines produced from laser-irradiated targets on the Orion laser facility. The instrument utilizes a spherically bent crystal geometry to spatially focus and spectrally analyze photons from foil or microdot targets. The high photon collection efficiency resulting from its imaging properties allow the instrument to be mounted outside the Orion chamber, where it is far less sensitive to particles, hard x rays, or electromagnetic pulses than instruments housed close to the target chamber center in ten-inch manipulators. Moreover, Bragg angles above 50^o are possible, which provide greatly improved spectral resolution compared to radially viewing, near grazing-incidence crystal spectrometers. These properties make the new instrument an ideal lineshape diagnostic for determining plasma temperature and density. We describe its calibration on the Livermore electron beam ion trap facility and present spectral data of the K-shell emission from highly charged sulfur produced by long-pulse as well as short-pulse beams on the Orion laser in the United Kingdom.

I. INTRODUCTION

High-power, short-pulse lasers have enabled the probing of matter under extreme conditions of density and temperature. Two exciting recent advances, which highlight the type of interesting science that can be done with short-pulse lasers, are the production of copious amounts of laser-generated, jet-like leptonic antimatter[1–3] and the production of hot, solid-density plasma near local thermodynamic equilibrium, which, for example, allows the observation of ionization potential depression[4–6]. Measurements of electron density and temperature are crucial for plasma characterization and, ultimately, for understanding the underlying physical processes and plasma control. X-ray spectroscopy has been a method of choice for making such measurements. Indeed, x-ray spectrometers have been used from the very onset of laser-produced plasma studies to diagnose the resultant plasma conditions[7]. X-ray spectrometers with sufficient resolving power have enabled the study of spectral line shapes in order to determine the electron density from the Stark broadening of a suitable x-ray line, while the electron temperature is inferred from the relative intensity of dielectronic satellite features[8–11].

High-power short-pulse lasers, such as the 527 nm, 100 J, 500 fs short-pulse beam on the Orion laser facility[12], add complexity to the diagnostic requirements. The size of the laser-produced plasma is small, i.e., it is typically well below 100 μm. The plasma radiates only for a short time, i.e., for a few to a few tens of picoseconds. These two properties combine so that the overall x-ray flux is rather small. However, the plasma is also hot (500 – 1000 eV) and dense (solid density), which increases the number of emitted photons, albeit not to the level typically seen from plasmas produced by present-day, large, long-pulse laser facilities.

In this paper, we describe the design and performance of a high-resolution crystal spectrometer designed specifically for the determination of plasma characteristics from the line shape of x-ray lines produced by the Orion laser. The instrument is dubbed the ORION high-resolution x-ray (OHREX) spectrometer. Its design features include the use of a bent-crystal geometry to collect the most light and concentrate it onto a small detector area to maximize signal to noise. It also includes the use of two crystals to cover two spectral bands simultaneously. The instrument is located outside the Orion target chamber for easy access and minimal exposure to hard x rays or energetic particles that can lead to a degradation

of the signal-to-noise ratio.

Spectrometers utilizing spherically bent crystals have been used before on short pulse laser produced plasma sources[13–15] and other micrometer-sized plasma sources, such as electron beam ion traps[16–18] and Z-pinch and X-pinch plasmas[19,20], mainly in order to increase the light gathering power from rather weak sources. As a result, these spectrometers were located close to the plasma source, and the Bragg angles were rather shallow to allow radial access, often within the vacuum chamber. However, the present design of OHREX derives from a spectrometer geometry originally developed for large-volume plasmas found in tokamaks[21–23] and was explored in a smaller-scale setup on the Titan laser at Livermore[24]. For example, the instrument design for the core-imaging x-ray crystal spectrometer for the ITER (Latin "the way") tokamak envisions a demagnification of the plasma by a 5:1 ratio to produce a one-dimensional, reduced image on a two-dimensional detector array, where the second dimension is the spectral axis[25]. By locating the micron-size laser-produced plasma source near the location of the sagittal (i.e. vertical) focus of such an instrument we can efficiently collect and concentrate the emitted light on the detector. The OHREX spectrometer maintains the roughly 5:1 demagnification of the ITER instrument. This means that the crystal can be located about 40 cm outside the 4 m diameter Orion vacuum chamber, while keeping the distance between the crystal and detector to about 50 cm. It also means that a Bragg angle near 45°, which has been envisioned for the ITER spectrometer[25], is maintained on OHREX. Unlike in tokamak observations, however, the relatively short distance between the crystal and the detector does not entail a loss in resolving power. The reason is that the minute source size of the Orion laser target suppresses the so-called Johann error[26], which represents the largest error contribution when investigating extended sources.

In the following we give details of the design of the OHREX spectrometer. This is followed by spectral calibration measurements on the Livermore electron beam ion trap and by spectral measurements from targets irradiated with Orion long-pulse and short-pulse beams in the United Kingdom.

II. IMAGING PROPERTIES OF OHREX

In the following we first discuss the general design characteristics of the OHREX instrument. Subsequently, we give the specific parameters, such as Bragg angles, crystal types,

and dimensions, which we employed when building our instrument.

A. General design considerations

A spherically bent crystal with radius of curvature R_c has four foci: two foci that describe the location of the images, and two that describe the location of the source. Two foci, the meridional, or horizontal, foci, are associated with spectral focussing. The equation for focusing meridional rays is given by

$$1/p_m + 1/q_m = 2/(R_c \sin\theta). \tag{1}$$

The other two foci, the sagittal, or vertical, foci, are associated with spatial focussing. The focussing equation for sagittal rays is given by

$$1/p_s + 1/q_s = 2\sin\theta/R_c. \tag{2}$$

In both cases, p and q are the distances of the source and the image foci, respectively. The angle of incidence is denoted by θ.

Unlike mirrors, crystals diffract photons according to Bragg's law

$$n\lambda = 2d\sin\theta. \tag{3}$$

Here λ is the wavelength of the incident x ray, n is the order of diffraction, and d is the lattice spacing of the crystal. The spectral focusing of a spherically bent crystal is the same as that of a cylindrically bent crystal in the Johann geometry[26], if we require that meridional rays are focused at the image focal distance

$$q_m = R_c \sin\theta. \tag{4}$$

X rays of wavelength λ that are incident on the crystal parallel to the plane of diffraction are, thus, focused to a point that lies on a circle of radius $R_c/2$. This circle is called the Rowland circle[27,28]. X rays with a different wavelength are focussed at a different point along the Rowland circle.

In order to maximize the signal-to-noise ratio of the diffracted x-ray signal on the detector we require that the sagittal x rays, which are oblique to the diffraction plane, are also focussed at the sagittal focus

$$q_s = R_c \sin\theta. \tag{5}$$

Other spectrometer designs, for example those for use on the National Ignition Facility[29], have not implemented such a requirement. However, we believe that it highly advantageous to concentrate the signal on the smallest possible area of the detector.

The requirement that $q_s = R_c \sin\theta$ means that the sagittal source focal distance equals

$$p_s = -R_c \sin\theta / \cos(2\theta). \tag{6}$$

This is ilustrated in Fig. 1. The figure shows that the sagittal source focal distance is a line focus. Similarly, the meridional source focal distance p_m is also a line focus, albeit rotated by 90° from the sagittal focus. Only the sagittal and meridional image foci at q_s and q_m, respectively, are, by design, point foci.

As seen from Fig. 1, the source focus of the sagittal rays and the source focus of the meridional rays do not coincide. They are, however, related by the equation

$$p_s = -p_m / \cos(2\theta). \tag{7}$$

In other words, source focussing of the sagittal rays, i.e., $p_s > 0$, is only achieved, if the Bragg angle is larger than 45°. For $\theta = 45°$ the sagittal rays are parallel, which means that their focus is at infinity. For $\theta < 45°$ the rays diverge, and the rays seem to emerge from a virtual sagittal focus behind the crystal.

OHREX operates at a Bragg angle larger than 45° so that the focussing conditions shown in Fig. 1 apply. If we place the x-ray source at the sagittal source focus p_s, then we can collect the light from all x rays that impinge on the crystal on a vertical strip of the crystal of height h_c. A taller crystal, thus, results in a larger collection of x rays. If the x-ray source is a point, then the width of the vertical strip is given approximately by the rocking curve of the crystal. This means that only a very narrow segment of the crystal contributes to the signal that is collected. A spatially extended source increases the effective width that contributes to the signal. In the limit of a very large source, such as a tokamak plasma, the entire crystal length l_c contributes to the signal collection.

The spectral resolving power $\lambda/\Delta\lambda$, which is critical for measuring the shape of a given line, is determined by the Johann error:

$$\Delta\theta = \frac{(l_c^{eff})^2}{8R_c^2 \tan\theta}. \tag{8}$$

Because of the diminutive size of the Orion x-ray source the effective length of the crystal l_c^{eff} that contributes to the signal is negligible compared to R_c, and the Johann error essentially

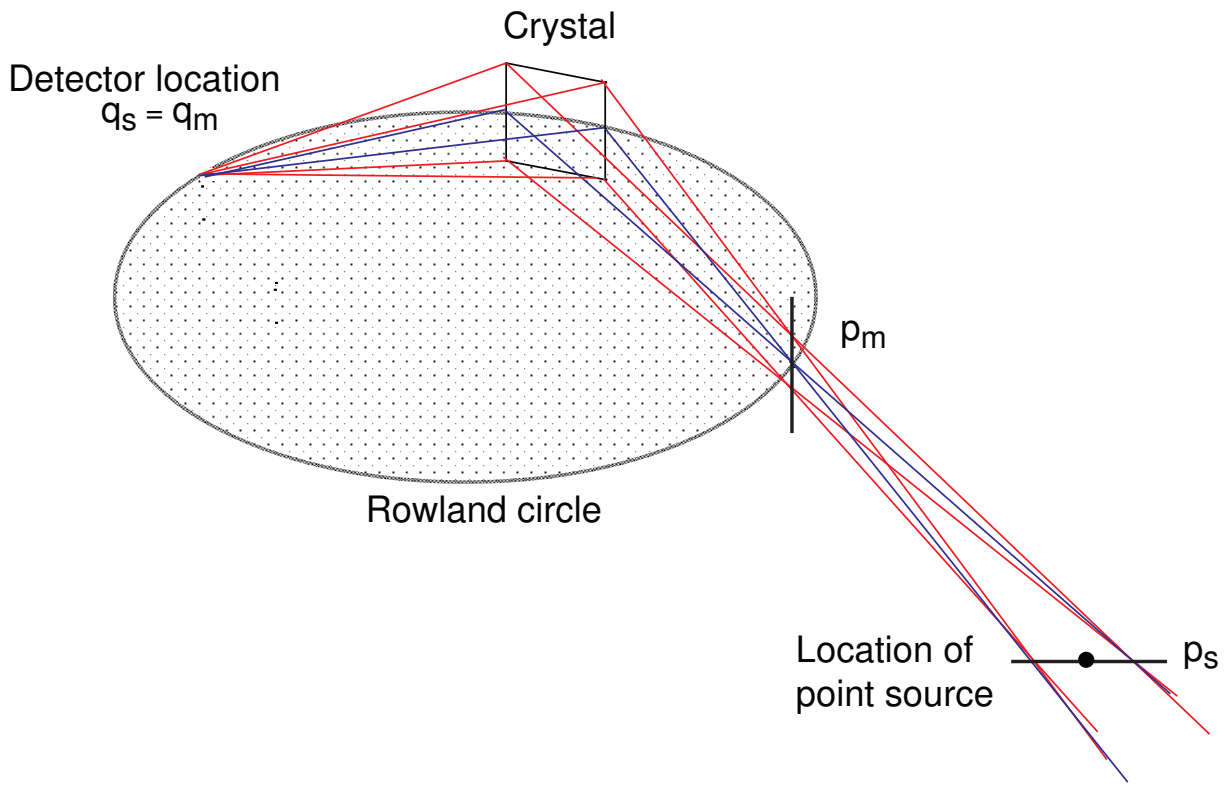

FIG. 1. Focussing properties of the spherically bent crystal used in the OHREX spectrometer. The sagittal and meridional image foci q_s and q_m, respectively, are set to equal $R_c \sin\theta$. This means that both the spectral and the spatial focus are on the Rowland circle. The second meridional focus p_m forms a line that is perpendicular to and intersects the Rowland circle. The second sagittal focus p_s also forms a line, which is in the plane of the Rowland circle.

vanishes. Instead, the limits on the spectral resolving power stem from the intrisic resolving power of the crystal itself and the quality of the bend.

Although a longer crystal does not increase the signal strength from Orion plasmas, a longer crystal is preferable because the length of the crystal determines the spectral range covered by the instrument. This is illustrated in Fig. 2.

Only x rays with wavelength λ_1 from a point source located at position "λ_1" on the Rowland circle shown in Fig. 2 will be focused on the detector. Similarly, x rays with wavelength λ_2 from a point source on the Rowland circle at located λ_2 will be focused on the detector. In other words, a point source on the Rowland circle will only produce a

monoenergetic signal. By placing the source away from the Rowland circle, as required by our focusing condition, a segment of the Rowland circle is illuminated, resulting in a finite energy coverage, as illustrated in Fig. 2. The range of energy is, thus, determined by the length of the crystal.

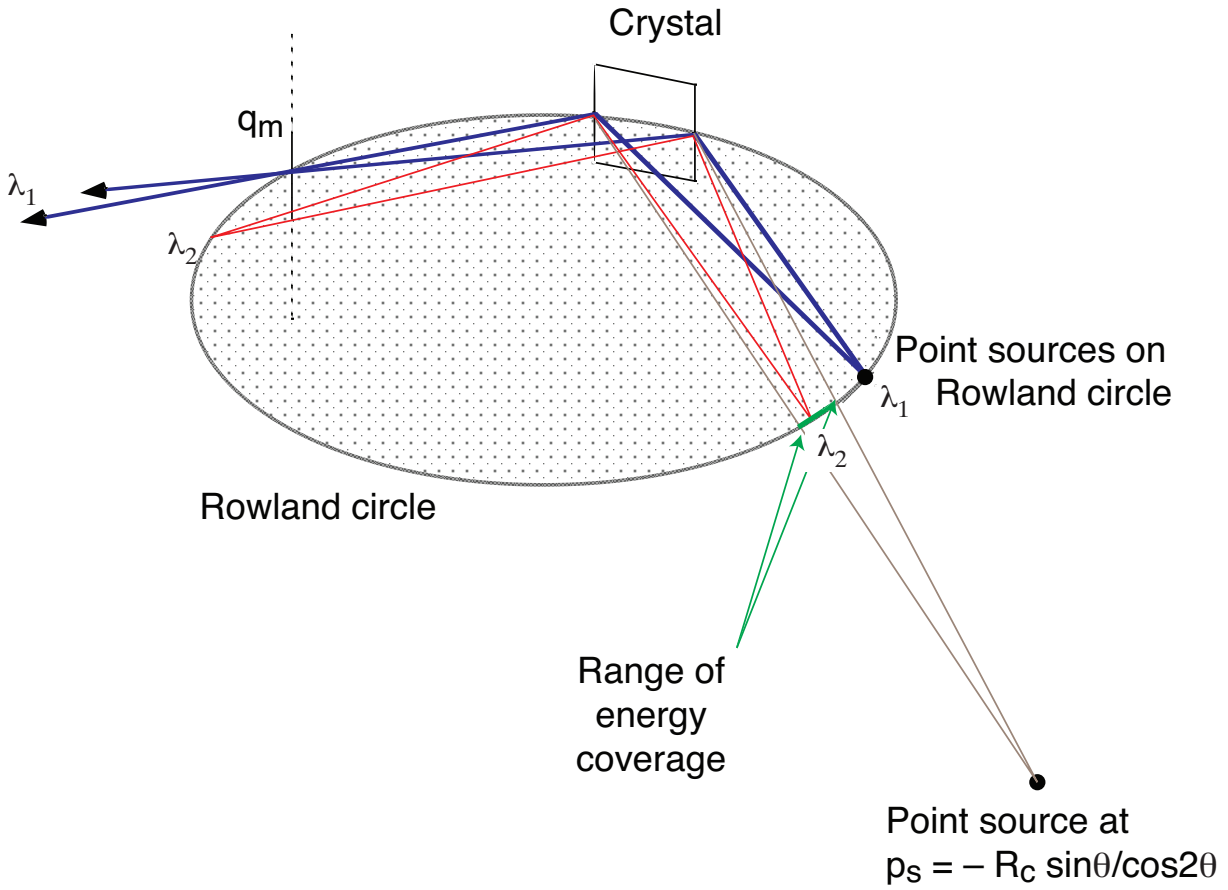

FIG. 2. Energy range coverage of the OHREX spectrometer by an x-ray point source located outside the Rowland circle.

B. Specific design parameters of the OHREX spectrometer

Density measurements based on the Stark broadening perferentially utilize K-shell x-ray transitions from levels with principal quantum number $n = 3$, i.e., the $3p \rightarrow 1s$ Lyman-β transitions in hydrogenlike ions or the $1s3p\ ^1P_1 \rightarrow 1s^2\ ^1S_0$ He-β transitions in heliumlike

ions. Density determinations on Orion[5,6], for example, have relied on the line shape of the He-β line of heliumlike Al^{11+} and of the Lyman-β line of hydrogenlike Al^{12+}. Hydrogenlike and heliumlike ions from elements with higher atomic number than aluminum extend such measurements to plasmas with higher electron temperature.

For use on Orion, we aimed at a spectrometer that can observe the relevant K-shell transitions for a range of elements starting from aluminum. We furthermore required that switching from one set of lines to another can be accomplished without time-consuming realignment of Bragg angles and focusing.

We have accomplished our goals by designing a spectrometer that has a fixed nominal Bragg angle of 51.3°. Different wavelength ranges are selected by implementing crystals with different lattice spacings d. For example, a quartz $(10\bar{1}0)$ crystal with $2d = 8.512$ Å allows us to measure the He-β line of Al^{11+} at 1869 eV, while a quartz $(21\bar{3}1)$ crystal with $2d = 3.082$ Å allows up to measure the He-β line of Sc^{21+} at 5070 eV. Similarly, the Lyman-β line at 2377 eV can be measured with a quartz $(10\bar{1}1)$ crystal with $2d = 6.697$ Å. An overview of several crystal cuts used in the OHREX spectrometer and the associated coverage of x-ray energies is given in Table I.

The fact that the nominal Bragg angle of the instrument remains fixed greatly reduces the effort to set up the spectrometer to different lines. In fact, OHREX accommodates two crystals simultaneously. A schematic of our setup is shown in Fig. 3. One crystal is attached to the bottom plate, the other on the top plate. (The top plate was removed in the illustration in Fig. 3, but the crystal was left in place for illustrational purposes. In reality, the crystal would have been removed together with the top plate.)

By virtue of having the same focal length, both crystals focus onto the same detector plane. This way the instrument can cover two spectral ranges at once. Moreover, because each crystal is installed together with its mounting plate, it can be aligned offline to the desired Bragg angle and inserted when needed. It is, therefore, possible to exchange crystals and access different spectral regions without *in situ* alignment or the need to refocus the detector.

Because a taller crystal will collect more light and a longer crystal will cover a wider energy range it is desirable to implement crystal with a large surface area. In OHREX we utilize crystals that are typically $h_c = 40$ mm tall and $l_c = 60$ mm long.

The radius of curvature is determined by our desire to place the plasma source at the

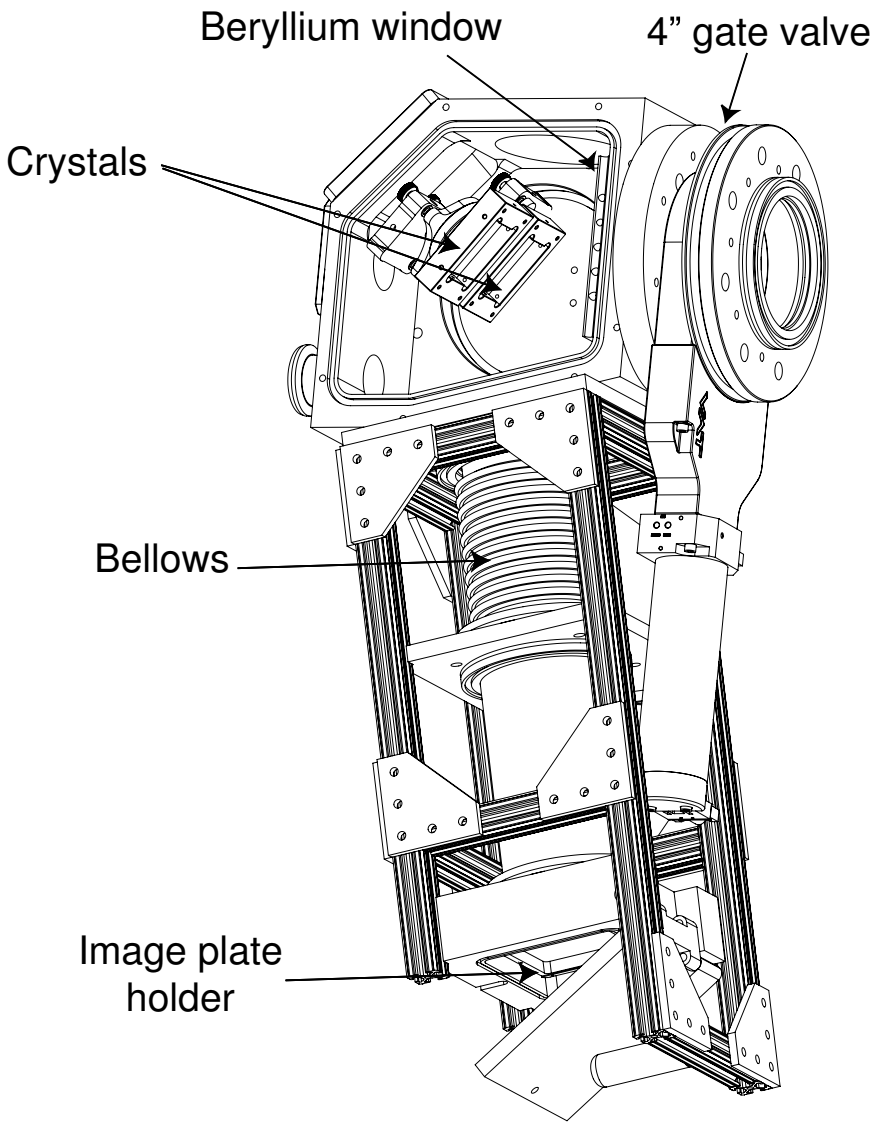

FIG. 3. Schematic of the OHREX spectrometer showing the location of the two crystals, the bellows that allow focussing of the detector plane, and the detector location, i.e. the image plate. A beryllium window located between the crystal and the gate valve serves as a light block.

sagittal focus p_s, as illustrated in Fig. 1, and by our desire to place the body of spectrometer on the outside of the Orion target chamber. The latter design feature means that the instrument can readily afford Bragg angles larger than 45°, which are desirable for measurements with high spectral resolution. It also means that the spectrometer is easily serviceable and that it is far removed from the source of electromagnetic pulses and hard x rays.

The Orion target chamber has a diameter of 4 m. In order to accommodate flanges and a gate valve we allow another 40 cm, so that the distance between the crystal and the

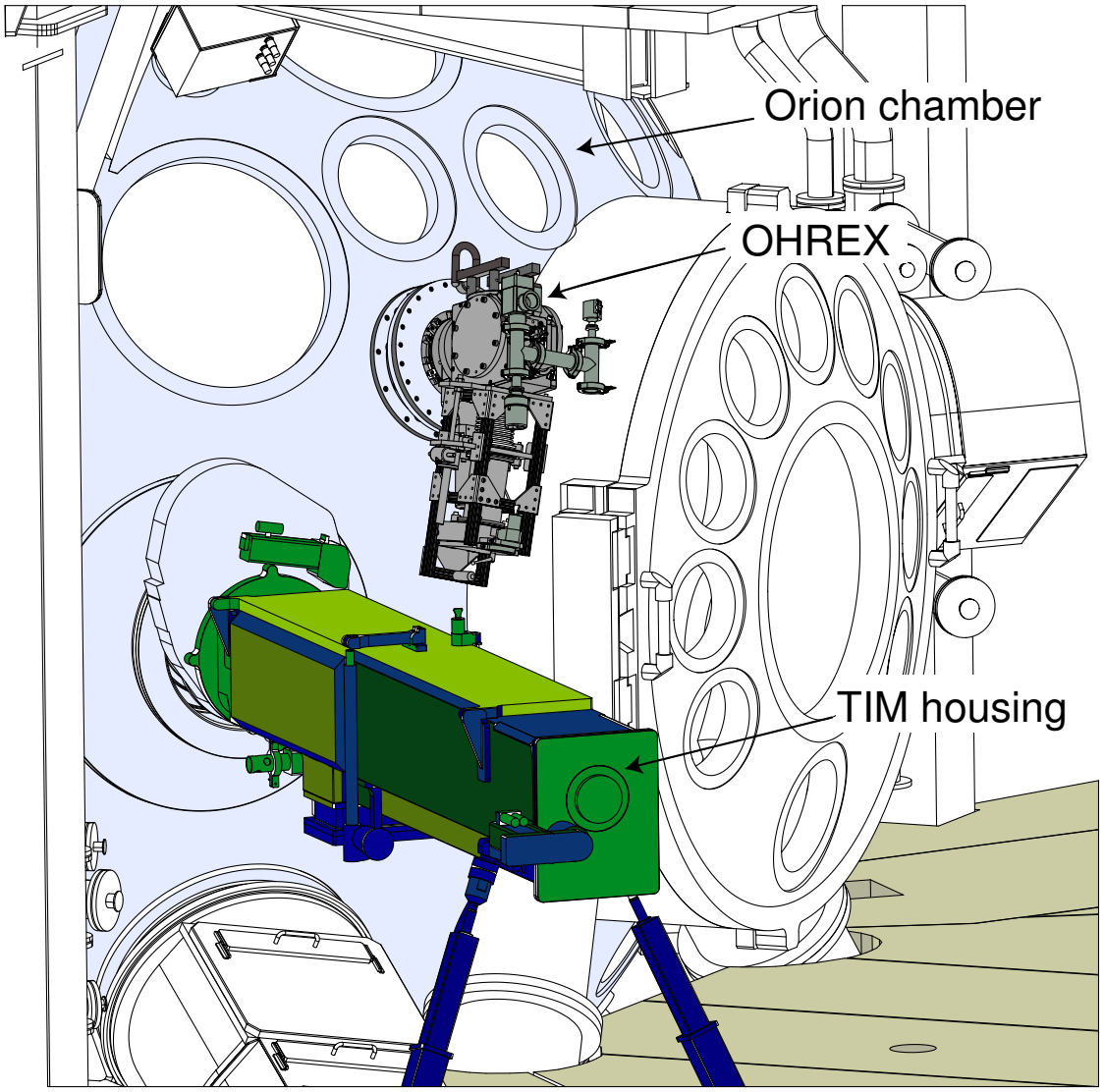

FIG. 4. Schematic of the OHREX spectrometer (shown in grey) mounted on the Orion laser chamber (shown in light blue). A Ten-Inch-Manipulator (TIM) module in green is shown for comparison.

plasma at target chamber center is $p_s = 240$ cm. This is illustrated in Fig. 4. Recalling that $p_s = -R_c \sin\theta / \cos(2\theta)$ we need to set $R_c = 67.2$ cm. It follows that the detector must be placed $q_s = 52.4$ cm from the center of the crystal.

Our 6 cm long crystals bent to a spherical radius of curvature $R_c = 67.2$ cm yield an energy coverage of a little over 6% at a nominal Bragg angle of $\theta = 51.3°$. As mentioned, the specific energy ranges covered by OHREX for selected crystals are listed in Table I.

Finally, we note that at the Bragg angle at which we operate OHREX a finite source

at p_s will be (mono-energetically) imaged at q_s with a (de-)magnification $M = 0.21$. The fact that the plasma source is demagnified means that its internal structure cannot be resolved, as most detectors do not have spatial resolution elements that are on the order of micrometers. For example, when operating on Orion, OHREX utilizes a 3" by 3" image plate as the detector. The typical spatial resolution of an image plate scanner is 75 μm, which is far larger than the 10 μm size of the demagnified image of the 50 μm diameter x-ray emitting spot produced by a short-pulse heated microdot target. Another limiting factor is the focus quality of a spherically bent crystal. We find that the spatial focus of our crystals varies from about 10 μm to 800 μm; for the present setup we have chosen crystals with the best imaging properties, as tested with sychrotron radiation and micro-focus x-ray tube measurements[30,31].

The fact that OHREX uses a spatially demagnifying geometry coupled with the fact that the source size itself is very small means that precise spatial focusing, i.e. precisely setting the distance p_s between the target and the crystal and the distance q_s between detector and crystal, is not critical. By contrast, one may assume that precisely setting the distance between detector and crystal is nevertheless highly critical for obtaining the best spectral focus, since the spectral focusing distance q_m needs to be set to equal the spatial focusing distance q_s. However, the spectral focus is very weakly dependent on the exact value of q_m because of the minute source size, which dramatically reduces the Johann error, as discussed in the previous subsection. Spectrally, OHREX behaves like a von Hámos spectrometer[32]; the only difference is that a true von Hámos spectrometer has a cylindrically bent crystal, while our instrument has a spherically bent crystal. As a consequence, our spectrometer design allows for great ease of use and for minimal effort to achieve the desired spectral and spatial focusing.

Spatial and spectral focussing is achieved by moving the detector. It can be translated along the crystal-detector axis by compressing or stretching the bellows shown in Fig. 3. The crystals themselves are mounted in a way that allows for adjusting the Bragg angle. Although the nominal Bragg angle is 51.3°, slight rotation of the crystal will set the central Bragg angle to different values so that somewhat higher or lower x-ray energy ranges can be measured than the nominal values given in Table I.

The crystal mount also allows us to change the tilt of the crystal. This gives us the ability to adjust the position of the spectral image on the detector. This feature is especially useful

for ensuring that the images from the two crystals fall on different areas of the detector.

III. SETUP AND TESTING ON THE LIVERMORE ELECTORN BEAM ION TRAP FACILITY

The Livermore electron beam ion trap facility, which includes the EBIT-I and SuperEBIT electron beam ion traps[33,34], is an ideal source for developing and testing spectrometers[35,36]. The facility can produce radiation from essentially any desired element and charge state. In the following we report on data from the SuperEBIT electron beam ion trap used for testing the OHREX spectrometer before it was installed on the Orion target chamber.

The radiation in EBIT-I or SuperEBIT is produced in the interaction between an electron beam and trapped ions. The electron beam is compressed by a 3 T magnetic field to a diameter of about 50 μm[37,38]. The source width is thus of similar width as the microdot plasma produced with the Orion short-pulse beam.

The electron beam traverses a 2 cm long trap region. This means that the x-ray emitting region is substantially extended in one direction. As a consequnce, OHREX was set up such that its plane of dispersion is perpendicular to SuperEBIT's electron beam. That way the spectral focussing properties are the same as they are on Orion, while the spatial focussing properties will concentrate the emitted x rays into a 4 mm long line on the detector.

We use a liquid nitrogen cooled, open-nose charge coupled device (CCD) for x-ray detection. The CCD has 1300 $\times$ 1340 pixels. The pixel area is 20 $\times$ 20 μm. Thus, the spatial resolution of the CCD is a few times better than that of an image plate and about an order of magnitude better than the spatial resolution of the position-sensitive proportional counters that have been typically used for x-ray measurements with flat or cylindrically bent crystal spectrometers on the Livermore electron beam ion traps[39–44].

Because CCD cameras are highly sensitive to visible light, we have made sure that the detector is not exposed to stray light generated by the electron beam or emanating from the hot electron gun assembly. A 50 μm thick beryllium window was inserted into the space between the crystal and the gate valve that can be used to isolate the spectrometer vacuum from that of SuperEBIT or the Orion target chamber (cf. Fig. 3). The diameter of the beryllium window is 10 cm, which means that it cannot withstand atmospheric pressure. The window is, therefore, mounted on an assembly that allows for evacuation from both

sides of the window through a tortuous path that suppresses light propagation.

The intrinsic resolving power $\lambda/\Delta\lambda$ of quartz crystals is very high, ranging from about 10,000 for crystals with the largest lattice spacing, i.e., for quartz $(10\bar{1}0)$, to well above 100,000 for crystals with small lattice spacings[14,45]. Bending a crystal to a small radius of curvature can reduce the intrinsic resolving power[14,46,47]. However, there is typically no discernable effect for $R_c \geq 30$ cm, and the radii of our crystals are well above this value. As a consequence, the intrinsic resolution of a given crystal is not the limiting parameter of OHREX's spectral resolution. By contrast, a poorly focussing crystal because of, for example, a non-uniform curvature will limit the spectral resolution that can be attained.

Provided the detector has been placed at the optimal focussing distance, the spectral line width observed with OHREX on SuperEBIT is determined by the Doppler motion of the trapped ions. Trapped ions have a finite temperature, the value of which is a function of such basic machine parameters as the electron beam current and the trapping potential[48–50]. Unless the SuperEBIT device is operated at very low currents and very shallow traps, both of which severely reduce the x-ray emission, the trapped ions have a temperature of a few hundred eV. Here, ions with a low charge typically have temperatures at the low end (near 100–250 eV), and ions with a high charge have temperatures at the high end of the temperature range (above 500 eV).

For testing OHREX's performance we measured the x rays from heliumlike and hydrogenlike silicon. SuperEBIT was operated with a trapping potential of 100 V, and a beam current of 146 mA. The beam energy was set to 9.7 keV. Silicon was injected into the trap as decamethyltetrasiloxan in vapor form at a gas injection pressure of 2.5×10^{-7} torr.

The spectrum obtained with OHREX's quartz $(10\bar{1}1)$ crystal is shown in Fig. 5. The prominent feature is the $3p \rightarrow 1s$ Lyman-β line of hydrogenlike Si^{13+}. Some weaker features are seen as well. These are from $1snp\ ^1P_1 \rightarrow 1s^2\ ^1S_1$ transitions in heliumlike Si^{12+} with $n = 5$ (labeled He-δ), $n = 6$ (labeled He-ϵ), $n = 7$ (labeled He-ζ), and $n = 8$ (labeled He-η).

The Lyman-β line splits into two components, i.e., the transitions $3p_{3/2} \rightarrow 1s_{1/2}$ and $3p_{1/2} \rightarrow 1s_{1/2}$. These two components are only 0.520 eV apart[51]. Nevertheless, the lines are sufficiently resolved in the spectra measured with OHREX on SuperEBIT to discern their individual contributions visually. Using a line fitting procedure we determined their widths to be 0.267 ± 0.025 eV.

If we assume that the measured line width is solely due to the Doppler motion of the ions

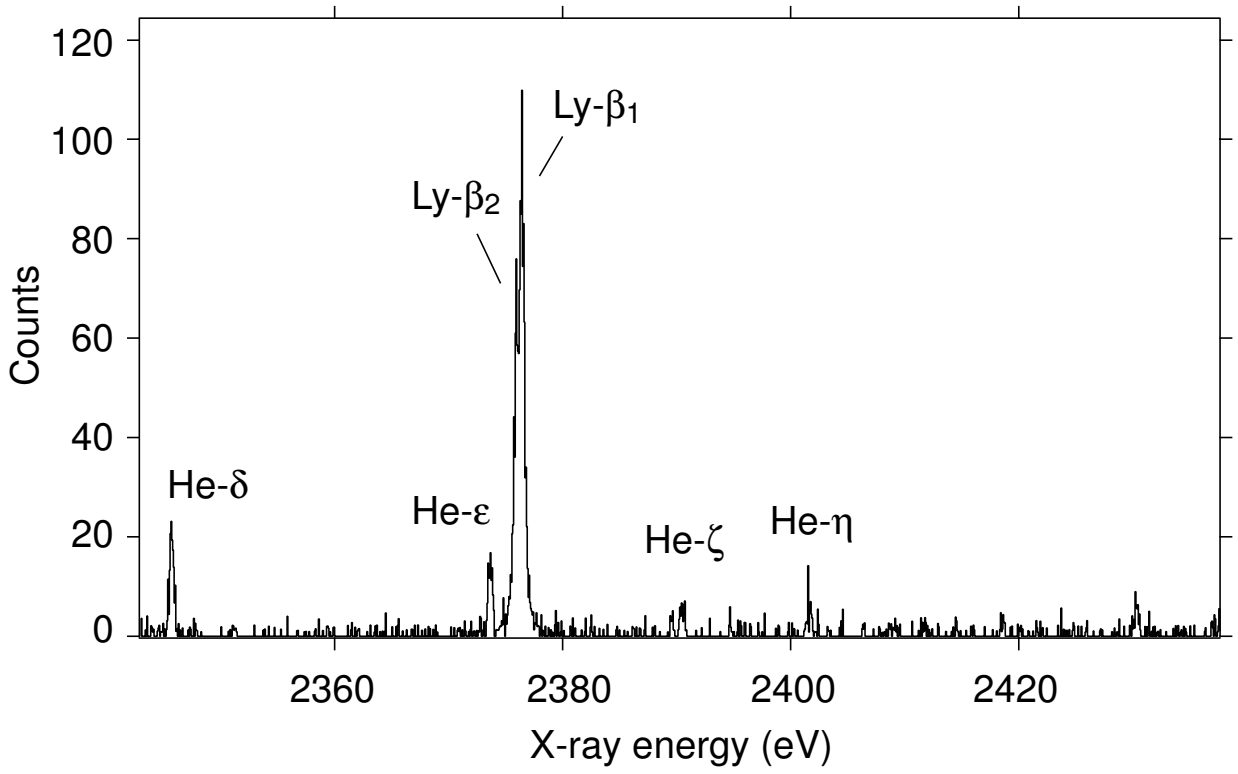

FIG. 5. K-shell transitions of heliumlike Si^{12+} and hydrogenlike Si^{13+} measured with OHREX at the Livermore SuperEBIT facilty. The spectrometer utilized a quartz $(10\bar{1}1)$ crystal. The labels refer to the $3p_{3/2} \rightarrow 1s_{1/2}$ (Ly-β_1) and $3p_{1/2} \rightarrow 1s_{1/2}$ (Ly-β_2) transitions in hydrogenlike Si^{13+} and the transitions from upper levels $1s5p\ ^1P_1$ (He-δ), $1s6p\ ^1P_1$ (He-ϵ), $1s7p\ ^1P_1$ (He-ζ), and $1s8p\ ^1P_1$ (He-η) to the $1s^2\ ^1S_1$ ground state in heliumlike Si^{12+}.

in the trap, we can infer an ion temperature $T_i = 162 \pm 34$ eV from the measured line width. This temperature is lower than that found in an earlier measurement involving the Lyman-α lines of hydrogenlike Mg^{11+}, which gave $T_i = 246 \pm 20$ eV[52]. The Mg^{11+} measurement was made with a flat crystal so that crystal focusing defects were absent. Since we measure an even lower temperature with OHREX, we presume that our assumption is correct that the line width is dominated by the ion motion. Thus, the focusing defects of the present spherical crystal must be considerably smaller than that implied by the observed spectral line width. In other words, the resolving power of the spectrometer must be better than $E/\Delta E \approx 9000$.

IV. OHREX SPECTROMETER INSTALLATION AND OPERATION ON ORION

The Orion facility at Aldermaston in the United Kingdom combines long-pulse (nanosecond) and short-pulse (picosecond) laser beam operation[12]. Ten, 500 J, 0.34 μm long-pulse beams and two, 500 J, 1.05 μm short-pulse beams are available. One of the two Orion short-pulse laser beams can be operated at the 0.53 μm second harmonic wavelength. This greatly increases the contrast by suppressing the prepulse inherent in conventional infrared laser systems[53] and enables efficient heating of solid targets[4,6,54]. In the following we present data recorded both from long-pulse and short pulse irradiated targets.

The OHREX spectrometer was installed on port number 5 as shown in Fig. 4 and equipped with an image plate instead of a CCD camera. Although we employ the spectrometer in the environment of an intense laser ($I > 10^{18}$ W/cm^2), which is associated with a high radiation background from fast particles and high-energy photons, we did not find it necessary to add shielding or collimators to OHREX.

The spectrometer is situated outside the Orion vaccuum vessel, i.e. far away from the target, which minimizes background flux. Moreover, the light block afforded by the beryllium window prevents fast particles from hitting the crystal. In addition, x rays are detected on an image plate whose plane is almost parallel to a radial line of sight, so that the cross section for a direct hit of hard x rays from the target is minimized. Indeed, the image plate registered few hard x-ray events.

To test the need for detector shielding we inserted a 9.5 mm thick tantalum plate between the vacuum vessel and the image plate holder. There was no discernable decrease of hard x ray hits on the image plate.

We optically checked the accuracy of the pre-aligned crystal settings. We removed the beryllium light block and irradiated the tip of a glass fiber positioned at the center of the vented target chamber with a green laser beam. Laser light scattered off the fiber tip was collected by the crystals and focused in the image plane. We observed the resulting line focus and spatial position by eye on a transparent tissue paper placed at the nominal image location in lieu of an image plate.

In Fig. 6 we show the spectral image recorded with the OHREX spectrometer on Orion. The image shows the spectra produced by the quartz $(10\bar{1}1)$ and quartz $(11\bar{2}0)$ crystals

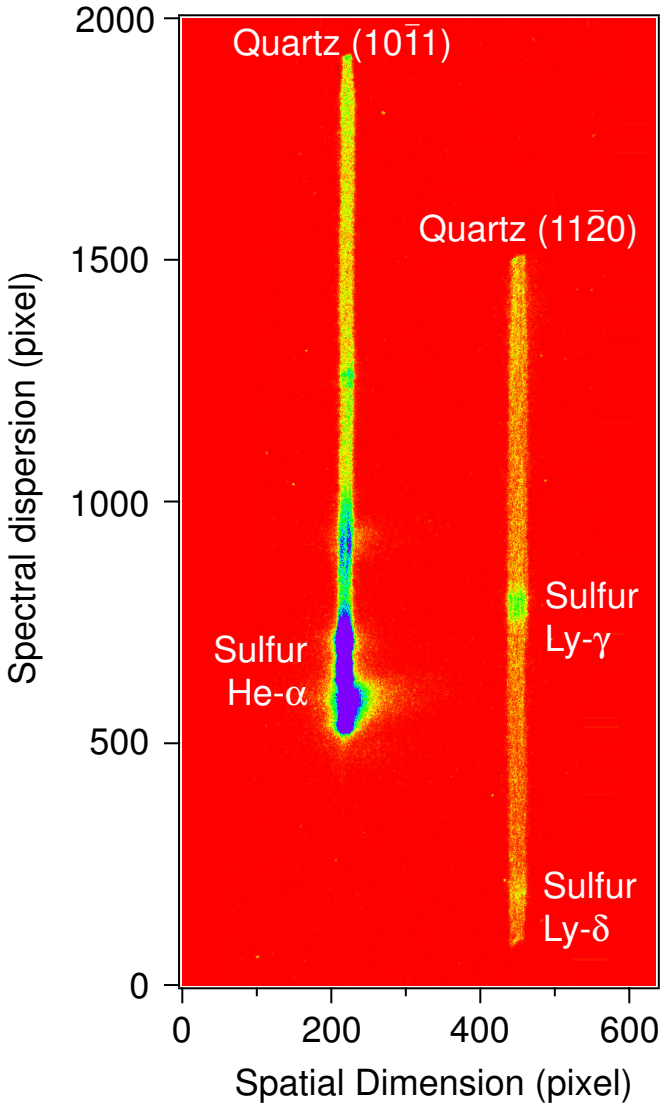

FIG. 6. Image of the spectra collected by the quartz (10$\bar{1}$1) and quartz (11$\bar{2}$0) crystals during shot no. 4826 of the Orion laser. The spectra were recorded from a long-pulse and short-pulse irradiated sulfonated plastic foil target and show the $n = 2 \rightarrow 1$ lines from heliumlike S^{14+} and the $n = 4 \rightarrow 1$ (Ly-γ) and $n = 5 \rightarrow 1$ (Ly-δ) lines of hydrogenlike S^{15+}. X-ray energy increases toward the bottom of the image.

from a long-pulse irradiated 25 μm thick foil target made of polyethersulfone. The 3ω pulse length was 0.5 ns, the beam energy was 224 J, and the spot size was 300 μm. The target was also hit by a 78 J 2ω beam with a 1.8 ps duration and 50 μm spot size.

The quartz (10$\bar{1}$1) image is dominated by the $1s2p\ ^1P_1 \rightarrow 1s^2$ line from heliumlike S^{14+}, labeled He-α or w; the quartz (11$\bar{2}$0) image displays the $n = 4p \rightarrow 1s$ and $n = 5p \rightarrow 1s$

lines of hydrogenlike S^{15+}. We note that the image plate was scanned perpendicular to the spectral direction to avoid pixel bleeding during scanning, which may otherwise compromise the spectral resolution.

The image in Fig. 6 illustrates the high signal-to-noise ratio that results from concentrating the spectrally dispersed x rays onto a narrow strip of the image plate. The width of the spatially focused spectrum is about 400 μm. This width represents the convolution of the spatial resolution of the image plate and scanner, of the focal quality of the crystal, and of the accuracy with which the image was focused. We stress that we did not attempt to focus the instrument while mounted on the Orion chamber and tighter spatial focusing may well have been achievable. However, there was no need to do so, unless we wanted to further improve the already excellent signal-to-noise ratio. The length of the spectral image is about 39 mm, or about 1.5 times the width of a typical CCD camera.

The high signal-to-noise ratio is ilustrated in Fig. 7(a), where we show a lineout of the spectrum of heliumlike S^{14+} produced by irradiating a polyethersulfone foil with a combination of short-pulse and long-pulse beams. In Fig. 7(b) we show a lineout of the spectrum of heliumlike S^{14+} produced by short-pulse-only irradiation of a 50 μm diameter sulfur microdot buried within two layers of parylene-N foil. The parylene foil is 2.5 μm thick on one side and 4 μm thick on the other side. The background is clearly higher in (b) than in (a), but the signal-to-background ratio is still very good. The long-pulse target irradiation results in a brighter signal than the signal observed during short-pulse-only target irradiation. The long-pulse beam lasts longer (500 ps) than the short-pulse beam ($\approx$ 1.2 ps). It also has more energy (242 J) and irradiates more material (spot size diameter 300 μm) than the short-pulse beam (73 J, 30 μm). The density in the buried microdot, short-pulse-only irradiated plasma is clearly higher, as the $1s2p\ ^3P_1 \rightarrow 1s^2$ intercombination line is suppressed by collisional quenching, as was observed in earlier measurements on the Titan short-pulse laser at Livermore[24].

V. OUTLOOK

We have demonstrated that OHREX has several advantages – high spectral resolution, good signal-to-noise ratio, and ease of use due to its location outside the Orion target chamber. Unlike other crystal spectrometers[55], OHREX does not compete for valuable real

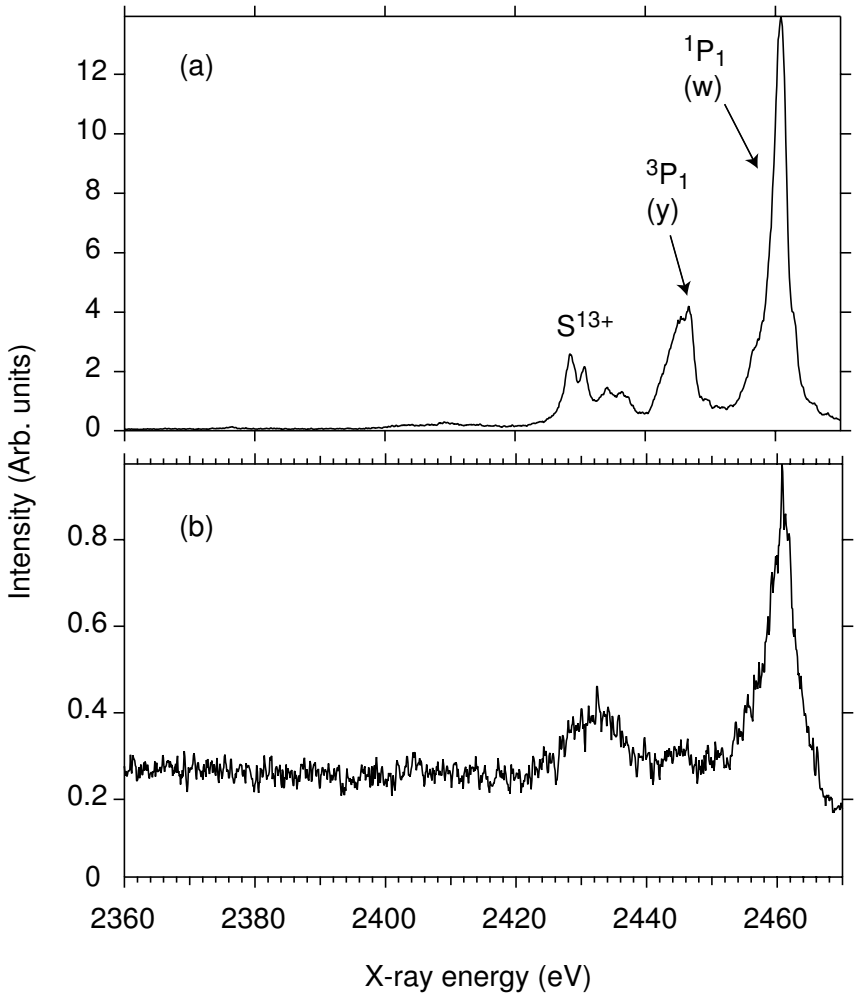

FIG. 7. Spectrum of heliumlike S^{14+} produced (a) by a long-pulse/short-pulse laser beam combination irradiating a foil target and (b) by a short-pulse only laser beam irradiating a buried microdot target. The data were collected with the quartz $(10\bar{1}1)$ crystal on the Orion laser during shots (a) no. 4842 and (b) no. 4862. The strongest feature represents the $1s2p\ ^1P_1 \rightarrow 1s^2\ ^1S_0$ transition. The so-called $1s2p\ ^3P_1 \rightarrow 1s^2\ ^1S_0$ intercombination line is only seen in the lower-density spectrum in (a).

estate inside a TIM tube.

Currently, the use of an image plate detector means that there is no time resolution. However, the spatial focusing afforded by OHREX is very well suited for coupling the spectrometer to a streak camera. Streak cameras with picosecond time resolution require a narrow entrance slit, and for highest efficiency x rays need to be concentrated onto the entrance slit[56,57]. A future upgrade to OHREX will, therefore, include outfitting it with a

streak camera.

ACKNOWLEDGEMENT

This work was performed under the auspices of the U.S. DOE by LLNL under contract under Contract DE-AC52-07NA27344. N. H. received support from the European Space Agency under contract No. 4000114313/15/NL/C3.

REFERENCES

[1]H. Chen, S. C. Wilks, J. D. Bonlie, E. P. Liang, J. Myatt, D. F. Price, D. D. Meyerhofer, and P. Beiersdorfer, Physical Review Letters **102**, 105001 (2009).

[2]H. Chen, S. C. Wilks, D. D. Meyerhofer, J. Bonlie, C. D. Chen, S. N. Chen, C. Courtois, L. Elberson, G. Gregori, W. Kruer, O. Landoas, J. Mithen, J. Myatt, C. D. Murphy, P. Nilson, D. Price, M. Schneider, R. Shepherd, C. Stoeckl, M. Tabak, R. Tommasini, and P. Beiersdorfer, Physical Review Letters **105**, 015003 (2010).

[3]H. Chen, D. D. Meyerhofer, S. C. Wilks, R. Cauble, F. Dollar, K. Falk, G. Gregori, A. Hazi, E. I. Moses, C. D. Murphy, J. Myatt, J. Park, J. Seely, R. Shepherd, A. Spitkovsky, C. Stoeckl, C. I. Szabo, R. Tommasini, C. Zulick, and P. Beiersdorfer, High Energy Density Physics **7**, 225 (2011).

[4]C. R. D. Brown, D. J. Hoarty, S. F. James, D. Swatton, S. J. Hughes, J. Morton, T. M. Guymer, M. P. Hill, D. A. Chapman, J. E. Andrew, A. J. Comley, R. Shepherd, J. Dunn, H. Chen, M. Schneider, G. Brown, P. Beiersdorfer, and J. Emig, Phys. Rev. Lett. **106**, 185003 (2011).

[5]D. J. Hoarty, P. Allan, S. F. James, C. R. D. Brown, L. M. R. Hobbs, M. P. Hill, J. W. O. Harris, J. Morton, M. G. Brookes, R. Shepherd, J. Dunn, H. Chen, E. Von Marley, P. Beiersdorfer, H. K. Chung, R. W. Lee, G. Brown, and J. Emig, Physical Review Letters **110**, 265003 (2013).

[6]D. J. Hoarty, P. Allan, S. F. James, C. R. D. Brown, L. M. R. Hobbs, M. P. Hill, J. W. O. Harris, J. Morton, M. G. Brookes, R. Shepherd, J. Dunn, H. Chen, E. Von Marley, P. Beiersdorfer, H. K. Chung, R. W. Lee, G. Brown, and J. Emig, High Energy Density Physics **9**, 661 (2013).

[7]D. J. Nagel, P. G. Burkhalter, C. M. Dozier, J. F. Holzrichter, B. M. Klein, J. M. McMahon, J. A. Stamper, and R. R. Whitlock , Phys. Rev. Lett. **33**, 743 (1974).

[8]B. A. Hammel, C. J. Keane, D. R. Kania, J. D. Kilkenny, R. W. Lee, R. Pasha, R. E. Turner, and N. D. Delameter, Rev. Sci. Instrum. **63**, 5017 (1992).

[9]B. A. Hammel, C. J. Keane, M. D. Cable, D. R. Kania, J. D. Kilkenny, R. W. Lee, and R. Pasha, Phys. Rev. Lett. **70**, 1263 (1993).

[10]C. J. Keane, B. A. Hammel, A. L. Osterheld, and D. R. Kania, Phys. Rev. Lett. **72**, 3029 (1994).

[11]R. C. Mancini, C. A. Iglesias, S. Ferri, A. Calisti, and R. Florido, High Energy Density Physics **9**, 731 (2013).

[12]N. Hopps, K. Oades, J. Andrew, C. Brown, G. Cooper, C. Danson, S. Daykin, S. Duffield, R. Edwards, D. Egan, S. Elsmere, S. Gales, M. Girling, E. Gumbrell, E. Harvey, D. Hillier, D. Hoarty, C. Horsfield, S. James, A. Leatherland, S. Masoero, A. Meadowcroft, M. Norman, S. Parker, S. Rothman, M. Rubery, P. Treadwell, D. Winter, and T. Bett, Plasma Physics and Controlled Fusion **57**, 064002 (2015).

[13]J. P. Geindre, P. Audebert, A. Rousse, J. C. Gauthier, A. Y. Faenov, T. A. Pikuz, S. A. Pikuz, and T. A. Shelkovenko, Phys. Scripta **53**, 645 (1996).

[14]T. Missalla, I. Uschmann, E. Förster, G. Jenke, and D. von der Linde, Review of Scientific Instruments **70**, 1288 (1999).

[15]T. A. Pikuz, A. Y. Faenov, A. I. Magunov, I. Y. Skobelev, F. Blasco, C. Stenz, F. Salin, P. Monot, T. Auguste, S. Dobosz, P. D'Oliveira, S. Hulin, and M. Bougeard, in *Applications of X Rays Generated from Lasers and Other Bright Sources II*, Vol. 4504 of *Proc. SPIE*, edited by G. A. Kyrala and J.-C. J. Gauthier (PUBLISHER, ADDRESS, 2001), pp. 14–25.

[16]Y. Aglitskiy, F. G. Serpa, E. S. Meyer, J. D. Gillaspy, C. M. Brown, A. Y. Faenov, and T. A. Pikuz, Phys. Scripta **58**, 178 (1998).

[17]N. Nakamura, A. Y. Faenov, T. A. Pikuz, E. Nojikawa, H. Shiraishi, F. J. Currell, and S. Ohtani, Rev. Sci. Instrum. **70**, 1658 (1999).

[18]D. L. Robbins, H. Chen, P. Beiersdorfer, A. Y. Faenov, T. A. Pikuz, M. J. May, J. Dunn, and A. J. Smith, Rev. Sci. Instrum. **75**, 3717 (2004).

[19]A. Y. Faenov, S. A. Pikuz, A. I. Erko, B. A. .Bryunetkin, V. M. Dyakin, G. V. Ivanenkov, A. R. Mingaleev, T. A. Pikuz, V. M. Romanova, and T. A. Shelkovenko, Physica Scripta **50**, 333 (1994).

[20]D. F. Wenger, D. B. Sinars, G. A. Rochau, J. E. Bailey, J. L. Porter, A. Y. Faenov, T. A. Pikuz, and S. A. Pikuz, Review of Scientific Instruments **77**, 10F312 (2006).

[21]M. Bitter, K. W. Hill, A. L. Roquemore, P. Beiersdorfer, S. M. Kahn, S. R. Elliott, and B. Fraenkel, Rev. Sci. Instrum. **70**, 292 (1999).

[22]M. Bitter, K. W. Hill, B. Stratton, A. L. Roquemore, D. Mastrovito, S. G. Lee, J. G. Bak, M. K. Moon, U. W. Nam, G. Smith, J. E. Rice, P. Beiersdorfer, and B. S. Fraenkel, Rev. Sci. Instrum. **75**, 3660 (2004).

[23]K. W. Hill, M. L. Bitter, S. D. Scott, A. Ince-Cushman, M. Reinke, J. E. Rice, P. Beiersdorfer, M.-F. Gu, S. G. Lee, C. Broennimann, and E. F. Eikenberry, Review of Scientific Instruments **79**, 10E320 (2008).

[24]H. Chen, M. Bitter, K. W. Hill, S. Kerr, E. Magee, S. R. Nagel, J. Park, M. B. Schneider, G. Stone, G. J. Williams, and P. Beiersdorfer, Review of Scientific Instruments **85**, 11E606 (2014).

[25]P. Beiersdorfer, J. Clementson, J. Dunn, M. F. Gu, K. Morris, Y. Podpaly, E. Wang, M. Bitter, R. Feder, K. W. Hill, D. Johnson, and R. Barnsley, J. Phys. B **43**, 144008 (2010).

[26]H. H. Johann, Z. Phys. **69**, 185 (1931).

[27]H. A. Rowland, Phil. Mag. **13**, 469 (1882).

[28]H. A. Rowland, Phil. Mag. Series 5 **16**, 197 (1883).

[29]J. A. Koch, R. E. Stewart, P. Beiersdorfer, R. Shepherd, M. B. Schneider, A. R. Miles, H. A. Scott, V. A. Smalyuk, and W. W. Hsing, Review of Scientific Instruments **83**, 10E127 (2012).

[30]K. W. Hill, M. Bitter, L. Delgado-Aparacio, P. Efthimion, N. A. Pablant, J. Lu, P. Beiersdorfer, H. Chen, and E. Magee, Review of Scientific Instruments **85**, 11D612 (2014).

[31]N. R. Pereira, A. T. Macrander, K. W. Hill, E. O. Baronova, K. M. George, and J. Kotick, Review of Scientific Instruments **86**, 103704 (2015).

[32]L. v. Hámos, Ann. der Physik **17**, 716 (1933).

[33]P. Beiersdorfer, E. Behar, K. R. Boyce, G. V. Brown, H. Chen, K. C. Gendreau, A. Graf, M.-F. Gu, C. L. Harris, S. M. Kahn, R. L. Kelley, J. K. Lepson, M. J. May, P. A. Neill, E. H. Pinnington, F. S. Porter, A. J. Smith, C. K. Stahle, A. E. Szymkowiak, A. Tillotson, D. B. Thorn, E. Träbert, and B. J. Wargelin, Nuclear Instruments and Methods in Physics Research B **205**, 173 (2003).

[34]P. Beiersdorfer, Can. J. Phys. **86**, 1 (2008).

[35]A. T. Graf, S. Brockington, R. Horton, S. Howard, D. Hwang, P. Beiersdorfer, J. Clementson, D. Hill, M. May, H. Mclean, R. Wood, M. Bitter, J. Terry, W. L. Rowan, J. K. Lepson, and L. Delgado-Aparicio, Can. J. Phys. **86**, 307 (2008).

[36]G. V. Brown, P. Beiersdorfer, J. Dunn, R. L. Kelley, C. A. Kilbourne, M. Leutenegger, E. Magee, J. Park, F. S. Porter, M. Schneider, and E. Träbert, Proc. SPIE **7732**, 77324Q (2010).

[37]M. A. Levine, R. E. Marrs, J. N. Bardsley, P. Beiersdorfer, C. L. Bennett, M. H. Chen, T. Cowan, D. Dietrich, J. R. Henderson, D. A. Knapp, A. Osterheld, B. M. Penetrante, M. B. Schneider, and J. H. Scofield, Nucl. Instrum. Methods **B43**, 431 (1989).

[38]S. B. Utter, P. Beiersdorfer, J. R. Crespo López-Urrutia, and K. Widmann, Nucl. Instrum. Methods **A 428**, 276 (1999).

[39]P. Beiersdorfer, R. E. Marrs, J. R. Henderson, D. A. Knapp, M. A. Levine, D. B. Platt, M. B. Schneider, D. A. Vogel, and K. L. Wong, Rev. Sci. Instrum. **61**, 2338 (1990).

[40]P. Beiersdorfer and B. J. Wargelin, Rev. Sci. Instrum. **65**, 13 (1994).

[41]D. Vogel, P. Beiersdorfer, V. Decaux, and K. Widmann, Rev. Sci. Instrum. **66**, 776 (1995).

[42]G. V. Brown, P. Beiersdorfer, and K. Widmann, Rev. Sci. Instrum. **70**, 280 (1999).

[43]D. Thorn and P. Beiersdorfer, Review of Scientific Instruments **75**, 3937 (2004).

[44]P. Beiersdorfer, G. V. Brown, R. Goddard, and B. J. Wargelin, Rev. Sci. Instrum. **75**, 3720 (2004).

[45]A. Burek, Space Sci. Instrum. **2**, 53 (1976).

[46]G. Hölzer, O. Wehrhan, J. Heinisch, E. Förster, T. A. Pikuz, A. Y. Faenov, S. A. Pikuz, V. M. Romanova, and T. A. Shelkovenko, Phys. Scripta **57**, 301 (1998).

[47]M. Sánchez del Rio, L. Alianelli, A. Y. Faenov, and T. Pikuz, Phys. Scripta **69**, 297 (2004).

[48]P. Beiersdorfer, V. Decaux, S. Elliott, K. Widmann, and K. Wong, Rev. Sci. Instrum. **66**, 303 (1995).

[49]P. Beiersdorfer, V. Decaux, and K. Widmann, Nucl. Instrum. Methods **B98**, 566 (1995).

[50]P. Beiersdorfer, A. L. Osterheld, V. Decaux, and K. Widmann, Phys. Rev. Lett. **77**, 5353 (1996).

[51]J. D. Garcia and J. E. Mack, J. Opt. Soc. Am. **55**, 654 (1965).

[52]P. Beiersdorfer, J. R. Crespo-López Urrutia, E. Förster, J. Mahiri, and K. Widmann, Rev. Sci. Instrum. **68**, 1077 (1997).

[53]D. Hillier, C. Danson, S. Duffield, D. Egan, S. Elsmere, M. Girling, E. Harvey, N. Hopps, M. Norman, S. Parker, P. Treadwell, D. Winter, and T. Bett, Applied Optics **52**, 4258 (2013).

[54]D. J. Hoarty, S. F. James, C. R. D. Brown, B. M. Williams, H. K. Chung, J. W. O. Harris, L. Upcraft, B. J. B. Crowley, C. C. Smith, and R. W. Lee, High Energy Density Physics **6**, 105 (2010).

[55]A. B. Steel, J. Dunn, J. Emig, P. Beiersdorfer, G. V. Brown, R. Shepherd, E. V. Marley, and D. J. Hoarty, Review of Scientific Instruments **85**, 11D610 (2014).

[56]R. Shepherd, P. Audebert, R. Booth, B. Young, J. Bonlie, D. Nelson, S. Shiromizu, D. Price, D. Norman, J. Dunn, K. Widmann, and P. Springer, Review of Scientific Instruments **75**, 3765 (2004).

[57]E. V. Marley, R. Shepherd, S. Fulkerson, L. James, J. Emig, and D. Norman, Review of Scientific Instruments **83**, 10E106 (2012).

TABLE I. Overview of x-ray lines accessible with OHREX using different crystals with a nominal Bragg angle of 51.3°.

Crystal cut	Quartz $(10\bar{1}0)$	Quartz $(10\bar{1}1)$	Ge (111)	Quartz $(11\bar{2}0)$	Quartz $(21\bar{3}1)$
$2d$	8.512 Å	6.697 Å	6.532 Å	4.912 Å	3.082 Å
Line of Interest	Al He-β (1869 eV)	Si Ly-β (2377 eV)	Si Ly-β (2377 eV)[a]	Cl He-β (3271 eV)	Sc He-β (5070 eV)
Energy coverage	1830–1950 eV	2330–2480 eV	2390–2540 eV	3180–3370 eV	5060–5380 eV

[a]With a slight adjustment of the crystal angle.